


Enhanced nanoscopy of individual CsPbBr₃ perovskite nanocrystals using dielectric sub-micrometric antennas

Cite as: APL Mater. 8, 021109 (2020); <https://doi.org/10.1063/1.5142225>

Submitted: 11 December 2019 . Accepted: 20 January 2020 . Published Online: 11 February 2020

Isaac Suárez , Thomas Wood , Juan P. Martinez Pastor , Dario Balestri, Simona Checcucci, Thomas David, Luc Favre , Jean-Benoît Claude , David Grosso, Andrés F. Gualdrón-Reyes , Iván Mora-Seró , Marco Abbarchi, and Massimo Gurioli

COLLECTIONS

Paper published as part of the special topic on [Light Emission from Perovskite Materials](#)

Note: This paper is part of the Special Issue on Light Emission from Perovskite Materials.



View Online

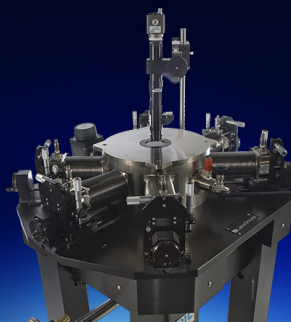


Export Citation



CrossMark

 **Lake Shore**
CRYOTRONICS



Cryogenic probe stations
for accurate, repeatable
material measurements

LEARN MORE 

AIP
Publishing

Enhanced nanoscopy of individual CsPbBr₃ perovskite nanocrystals using dielectric sub-micrometric antennas

Cite as: APL Mater. 8, 021109 (2020); doi: 10.1063/1.5142225
Submitted: 11 December 2019 • Accepted: 20 January 2020 •
Published Online: 11 February 2020



Isaac Suárez,^{1,2}  Thomas Wood,³  Juan P. Martinez Pastor,¹  Dario Balestri,^{4,5}  Simona Checcucci,^{4,5,6,a)}  Thomas David,^{6,b)}  Luc Favre,⁶  Jean-Benoît Claude,⁶  David Grosso,⁶  Andrés F. Gualdrón-Reyes,^{7,8,9}  Iván Mora-Seró,⁷  Marco Abbarchi,^{6,c)}  and Massimo Gurioli^{1,6,c),d)} 

AFFILIATIONS

- ¹UMDO, Instituto de Ciencia de los Materiales, Universidad de Valencia, Valencia 46071, Spain
²Escuela Técnica Superior de Ingenieros de Telecomunicación, Universidad Rey Juan Carlos, 28943 Madrid, Spain
³Institut de Nanotechnologies de Lyon, Ecole Centrale de Lyon, CNRS (UMR 5270), 69134 Ecully, France
⁴European Laboratory for Nonlinear Spectroscopy (LENs), 50019 Sesto Fiorentino, Italy
⁵Dipartimento di Fisica ed Astronomia, Università degli Studi di Firenze, 50019 Sesto Fiorentino, Italy
⁶Aix Marseille Univ., Université de Toulon, CNRS, IM2NP, Marseille, France
⁷Institute of Advanced Materials (INAM), University Jaume I, Avenida de Vicent Sos Baynat, s/n, 12071 Castelló de la Plana, Spain
⁸Centro de Investigaciones en Catálisis (CICAT), Universidad Industrial de Santander, Piedecuesta, Santander C.P. 681011, Colombia
⁹Faculty of Basic Sciences, University of Pamplona, Biofuels Lab-IBEAR, Pamplona C. P. 543050, Colombia

Note: This paper is part of the Special Issue on Light Emission from Perovskite Materials.

^{a)} **Present address:** INO-CNR, via G. Moruzzi, 1-56124 Pisa, Italy.

^{b)} **Present address:** X-FAB France SAS 224, Boulevard John Kennedy, 91105 Corbeil-Essonnes Cedex, France.

^{c)} **Authors to whom correspondence should be addressed:** marco.abbarchi@im2np.fr and gurioli@fi.infn.it

^{d)} **Permanent address:** Dipartimento di Fisica ed Astronomia, Università degli Studi di Firenze, 50019 Sesto Fiorentino, Italy.

ABSTRACT

We demonstrate an efficient, simple, and low-cost approach for enhanced nanoscopy in individual green emitting perovskite (CsPbBr₃) nanocrystals via TiO₂ dielectric nanoantenna. The observed three- to five-fold emission enhancement is attributed to near-field effects and emission steering promoted by the coupling between the perovskite nanocrystals and the dielectric sub-micrometric antennas. The dark-field scattering configuration is then exploited for surface-enhanced absorption measurements, showing a large increase in detection sensitivity, leading to the detection of individual nanocrystals. Due to the broadband spectral response of the Mie sub-micrometric antennas, the method can be easily extended to electronic transitions in other spectral regions, paving the way for absorption nanoscopy of many different quantum emitters from organic molecules to quantum dots.

© 2020 Author(s). All article content, except where otherwise noted, is licensed under a Creative Commons Attribution (CC BY) license (<http://creativecommons.org/licenses/by/4.0/>). <https://doi.org/10.1063/1.5142225>

INTRODUCTION

In the last decade, interest in semiconductors has seen a huge shift toward perovskites, with both the scientific community and industrial stakeholders attracted by the astonishing progress in the efficiency of perovskite solar cells.^{1–4} More recently, the

usage of metal halide perovskite nanocrystals (PNCs) in other conventional optoelectronic devices (e.g., LEDs,³ LASERS,⁵ and light detectors⁶) has come to fruition due to their superior absorption,³ emission,⁵ and nonlinear optical response,⁷ thus extending the range of interest in these materials in photonics. It is now possible to fine-tune the composition, structure, and size of the NCs

not only during synthesis but also via postsynthesis transformations. All this progress demands spectroscopic studies with spatial resolution able to address single NCs, that is, below the diffraction limit and with enhanced sensitivity. This is the realm of optical nanoscopy, which is of utmost relevance for many different fields, ranging from basic science to applications including materials science, photonics, biophysics, and quantum technologies. Recently, plasmonic nano-antennas, which have proven efficient nanoscopy tools for enhancing near-field to free-propagating radiation conversion, and vice-versa,^{8–15} have emerged to play a central role in this context. Some of the key aspects of the plasmonic nanostructures' success are easy implementation/engineering of different antenna architectures, broadband response, and nanoscale field confinement. On the contrary, one of their main limitations at visible and near-infrared frequencies is the large non-radiative loss due to energy dissipation by electron motion in metals.

A viable solution to overcome the strong Ohmic loss in metals is to exploit all-dielectric, sub-micrometric antennas (dielectric Mie resonators) for nanoscale light management.^{16,17} This distinct approach emerged in 2007 with SiC-based nanowires¹⁸ for infrared frequencies and more recently, since 2011, was extended to visible and near-infrared light with sub-micrometric structures (e.g., spheres, cylindrical pillars) based on group-IV semiconductors (e.g., Si and Ge).¹⁹ In this sense, a plethora of remarkable properties and applications have emerged, making this approach a valuable tool for light management with dielectric metasurfaces: structural color,²⁰ sensing,²¹ non-linear phenomena,²² anti-reflection coatings,²³ mirrors,²⁴ lenses,²⁵ polarizers,²⁶ and wave-front shaping¹⁶ are a few examples of ultra-thin devices.²⁷ Mie sub-micrometric antennas for PL enhancement of quantum dots have also been demonstrated²⁸ with lithographic structured Si disks, showing that the spectral overlap of electric and magnetic dipolar modes at the desired spectral range provides the optimal condition for PL angular steering. The integration of perovskites with Mie antennas is an emerging field in the optoelectronics community. Recent results demonstrated that the perovskite emission in polycrystalline thin films can be significantly enhanced by silicon sub-micrometric particles²⁹ or by nanoimprinting a metasurface directly into the perovskite thin film.³⁰ In addition, Mie resonances present in relatively large perovskite quasi-spheres were exploited to tune the emission wavelength³¹ or generate Fano resonances.³² Indeed, the use of perovskite materials has been recently reviewed as potential candidates to develop a new generation of "active metadevices."³³ To the best of our knowledge, the use of separate dielectric antennas coupled with PNCs to facilitate optical nanoscopy via a hybrid PNC–Mie system has not been studied yet.

In this work, we demonstrate the strength of broadband and lossless dielectric sub-micrometric antennas for nanoscopy of individual PNCs with a simple and low-cost method. We exploit a high-throughput fabrication method based on aerosol-spray to form quasi-perfect sub-micrometric spheres of polycrystalline titania (anatase form). The latter can be easily integrated into many systems for emission enhancement and steering, as well as absorption nanoscopy of single nanostructures. We successfully integrated CsPbBr₃ PNCs together with TiO₂ spheres, coupling the Mie resonances with the excitonic absorption and photoluminescence of the nanocrystals. We show that, even with the simplest possible photonic device architecture, i.e., consecutive deposition of Mie

resonators and PNCs onto a glass slide and without any further optimization, an average increase of the PL emission of single PNCs by a factor of three to five is achieved. Furthermore, guiding white light in the glass slide supporting PNCs attached/coupled to Mie resonators and exploiting the efficient near- to far-field scattering of light mediated by the sub-micrometric antennas, we obtain large absorption signals (up to 70%), whereas in conventional transmission measurements the PNCs' absorption edge is less than 0.1%. Numerical simulations are in agreement with the experimental results, paving the way for exploiting dark-field methods associated with near-field exciton–photon coupling mediated by all-dielectric optical resonators for nanoscopy in the world of quantum emitters.

RESULTS AND DISCUSSION

Titania-based Mie resonators and CsPbBr₃ PNCs were prepared by following well-established, high-throughput methods.³⁴ The PNCs were grown by following the hot-injection method developed by Protesescu *et al.*,² after convenient modifications detailed elsewhere.³⁵ The PNCs presented a cubic shape with an average size (L) of 11.8 nm, which is close to the Bohr radius (a_0) of the exciton in the corresponding bulk material (7 nm).² Then, the ratio $L/2a_0$ (L is the nanocube edge size) is 0.84, which corresponds to a weak quantum confinement regime. The receiving substrate for the titania spheres and PNCs was either a glass slide (for optical spectroscopy) or a Si wafer for scanning electron microscopy (SEM). The titania spheres and PNCs on either silica or silicon substrates were prepared with the same process, thus providing nominally identical samples. Detailed discussion of the experimental methods is provided in the Experimental Methods section.

Structural properties of titania spheres were assessed by high-resolution SEM imaging accounting for an almost perfect spherical shape [the difference in horizontal and vertical diameters is below 2%; Fig. 1(a)]. The sphere diameter, evaluated over more than 50 objects, spans from 50 nm to 400 nm, with the more probable value around 130 nm [Fig. 1(b)]. This guarantees a good antenna effect in the visible spectral region, as demonstrated later by the numerical simulations.

The optical properties of individual Mie resonators are assessed by standard dark-field microscopy and spectroscopy. Here, we exploited a lateral injection of white light undergoing total internal reflection within the glass substrate, providing a convenient dark-field setup for optical characterization by simply detecting the scattering in the far-field [Fig. 1(c)]. We limit our study to the range 400 nm–700 nm due to the green excitonic transition of CsPbBr₃ PNCs. Indeed, from the morphological data and comparing with previous reports,³⁴ we estimate that we only cut off scattering from the spheres having diameters below ~80 nm; these very small particles are quite rare in our ensemble and not relevant for antenna effects on the selected PNCs. It is also worth stressing that titania has an absorption edge around 370 nm.

We now address the properties of PNCs. Morphological characterization by SEM reveals the possibility of either an individual PNC (their shape is typically cubic or parallelepipedal, as expected for these kinds of systems)² or small clusters with two or a few PNCs [see the inset of Fig. 2(a)]. A statistical analysis [over more than 500 nano-objects; Fig. 2(a)] accounts for a preferential formation of

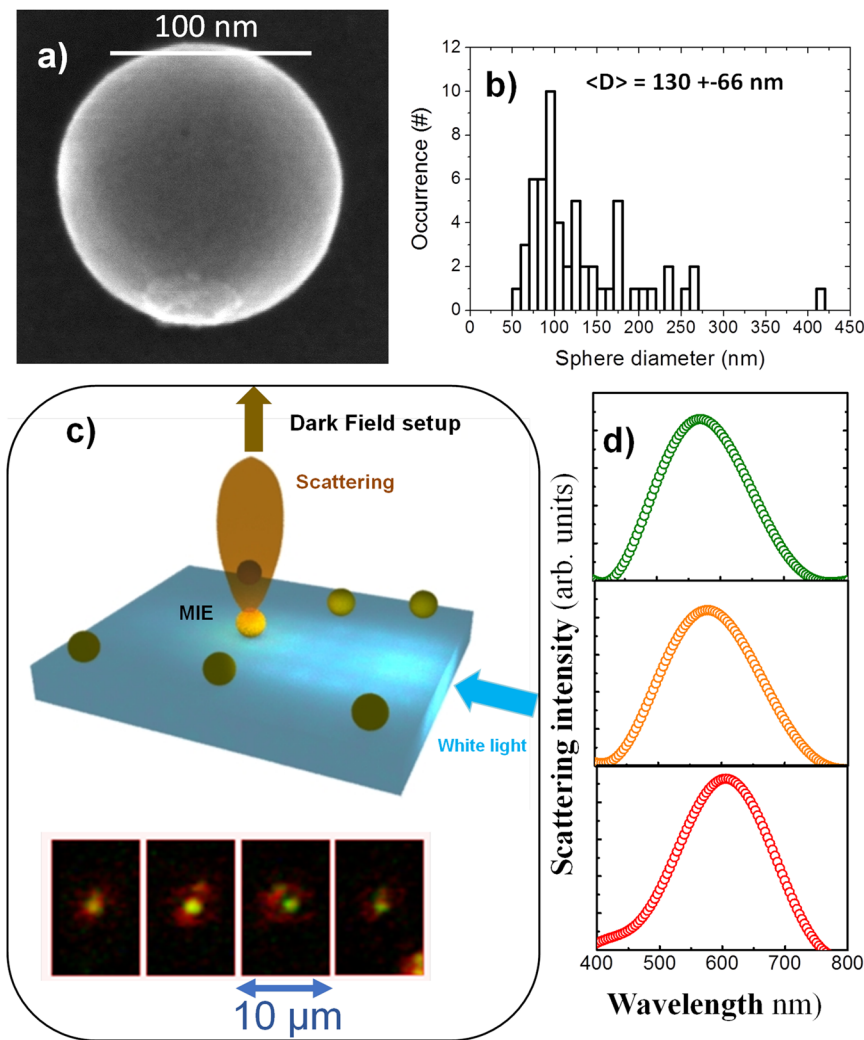


FIG. 1. (a) High-resolution SEM image of a spherical titania-based Mie resonator. (b) Statistical distribution of sphere diameter. (c) Top: Schematic of the illumination/detection of light scattering from Mie resonators on a glass slide (the scattering angular pattern is not calculated; it is just a guide for the eye). Bottom: Examples of light scattering from individual spheres detected with an optical microscope (50 \times , NA = 0.42); a residual chromatic aberration of our homemade detection system results in a two-color image. (d) Examples of dark-field spectra from individual spheres (not corrected for the lamp spectrum and detection spectral line-shape; for more details, see Ref. 34).

individual particles (~70% of the cases) rather than small clusters (~30% of the cases). In this sample, the size of the PNCs can range between a few tens of nm for individual PNCs (around 30 nm on average) to ≥ 100 nm for small clusters.

Standard transmission measurements are performed on a sample with high PNC density in order to check its absorption properties in the far-field. The absorption edge measured on the ensemble is located in the region 510–530 nm [Fig. 2(b)] in agreement

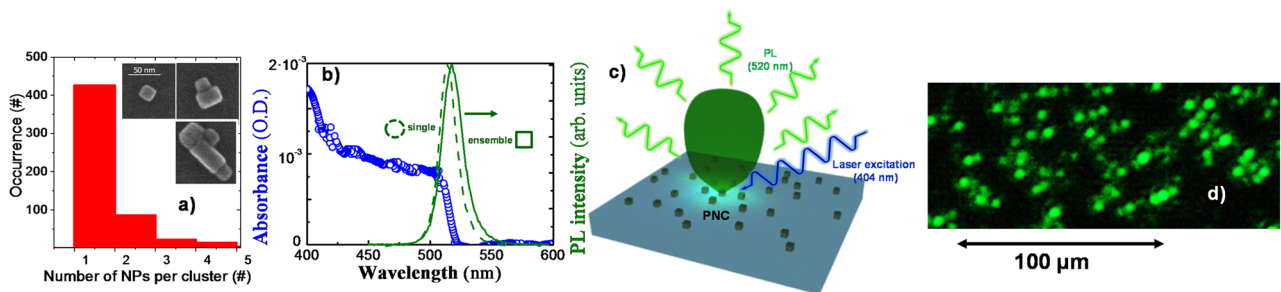


FIG. 2. (a) Statistics of the number of PNCs per cluster. Inset: High resolution SEM images of PNC clusters. (b) Optical density (blue circles, left axis) and PL intensity (green lines, right axis) as a function of wavelength. The PL spectra display the case of a single PNC (dashed line) and of the ensemble (continuous line). (c) Schematic of the PL setup. (d) Image of PL emission acquired with a CMOS color camera.

with the results reported in a previous publication for similar CsPbBr₃ PNCs;² the detected absorbance at the edge of the excitonic transition is quite small (in the range of 10^{-3}).³⁶

The PL spectrum integrated over a large ensemble of PNCs features an inhomogeneous broadening of about 20 nm in full width at half maximum (FWHM), only 2 nm larger than that of an individual emitter [Fig. 2(b)]. However, slightly different central wavelengths are found for the individual PNCs' emission, spanning ~15 nm (from 515 nm to 530 nm; see also Fig. 3). This comparison reveals a very small inhomogeneous broadening, thereby excluding significant quantum confinement (size-related) effects, as expected for our relatively large PNCs. Tentatively, we assign the inhomogeneity either to a residual size effect in the smallest CsPbBr₃ nanocrystals or, more likely, to the interaction with the substrate and its possible charged defects in analogy with the well-known spectral diffusion in III-V Quantum Dots.³⁷ We will exploit this inhomogeneity later in order to assess the enhancement in absorption sensitivity and spatial resolution in our nanoscopy approach.

We also note a reduced Stokes shift of ~5 nm (24 meV) between the excitonic PL emission band and the absorption edge of the PNCs, in agreement with the results reported for nanocrystals with similar size (11.8 nm).³⁸ It is worth mentioning that according to the theoretical predictions recently reported,³⁹ Mie resonances within individual PNCs of this size are expected to be neglected. Here, PL spectra were measured by laser excitation of the PNCs in backscattering geometry [Fig. 2(c)]. Wide-field imaging of PL emission in a sample with a high-density PNCs ensemble [Fig. 2(d)] demonstrates the possibility of individual emitter spectroscopy with a confocal setup.³⁷

PNCs are coupled to Mie resonators by successive depositions of both structures on the same glass slide. Morphological analysis

was performed by high-resolution SEM, simultaneously detecting titania spheres and PNCs. Quite often, the PNCs tend to localize at the bottom of the spheres [examples with one, two, and three PNCs are shown in the inset of Fig. 3(a)]. This likely has some analogy with the coffee-ring effect, which originates from a different evaporation rate across a solvent drop.⁴⁰ The resulting capillary flow carries the dispersed PNCs to self-assemble along the drop perimeter during the drying process.⁵ A statistical investigation over 64 objects (in a sample with a deposition protocol allowing high areal density of PNCs) reveals that about ~60% of the spheres are left without any PNCs, whereas in the other cases, more than half of the spheres are coupled with an individual PNC [Fig. 3(a)]. These numbers can change depending on the density of PNCs in the solvent, but they point out that we get a relatively large number of Mie resonators coupled to a PNC despite our straightforward and non-deterministic approach.

We perform a combined PL and dark-field scattering experiment on this PNC–Mie antenna coupled system [a sketch of the setup is provided in Fig. 3(b)] directly comparing the two wide-field views, the elastic scattering dominated by Mie resonators and the PL emission from PNCs [Figs. 3(c) and 3(d), respectively]. For the sake of better comparison, we have drawn white dashed circles around the points where strong elastic scattering is observed, that is, the points where the titania spheres are present. The same circles have also been drawn in the corresponding PL image. This analysis shows that either the PL is absent in the white circle or it is more intense with respect to the other spots. Also note that we performed this matching in real-time, superimposing the two excitations for a better correlation between the two optical signals.

In order to put these observations on a quantitative ground, we performed a statistical investigation of PL intensity of PNCs lying in the same place as a titania sphere (i.e., inside a white dashed

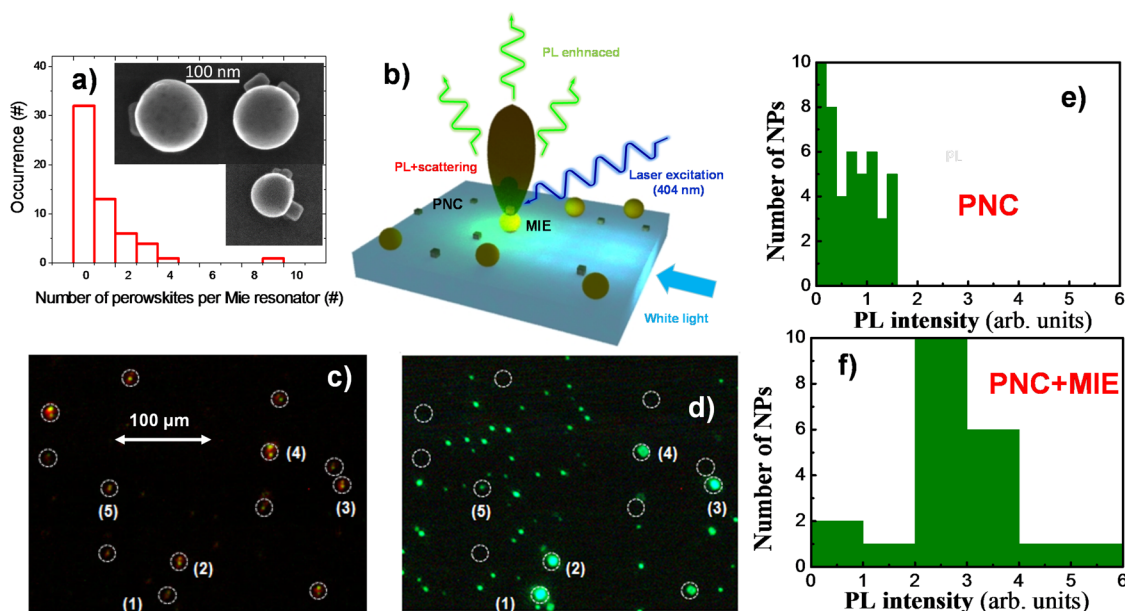


FIG. 3. (a) Statistics of the number of PNCs per Mie resonator. Inset: Example of SEM images. (b) Experimental setup; note that here the sizes of PNC and titania spheres are not to scale and the scattering patterns are just guide for the eye. (c) Dark-field image of the scattering of the Mie particles. (d) Dark-field image of the PL emission. (e) Statistics of the PL intensity emitted by individual PNCs. (f) Statistics of the PL intensity emitted by the PNCs+Mie system.

circle) over about 20 cases, and also of PL intensity of PNCs on different points with respect to the Mie resonators (i.e., outside the white dashed circles) over about 40 cases [Figs. 3(e) and 3(f), respectively]. The statistical investigation highlights a clear enhancement of the emission for PNC (or PNCs) coupled to titania nanospheres. Note that the PL spot inside the white circles does not guarantee the perfect coupling between PNCs and Mie resonators owing to the poor resolution of the optical measurements. Thus, in the statistics of the PL intensity from the PNC + Mie resonators, we likely include spurious data of PNCs not coupled to a titania sphere [e.g., those exhibiting an enhancement below two in our arbitrary units in Fig. 3(f)]. Nonetheless, the PL enhancement promoted by the antennas is of the order of three to five, indicating the confinement of a strong near field and preferable directionality perpendicular to the surface. Indeed, this effect is (qualitatively and quantitatively) similar to the surface enhanced fluorescence (SEF) observed for single molecules coupled to metallic antennas (gold nanoparticles) in the literature.^{41,42} However, a higher enhancement of PL is expected in our system due to the reduced attenuation of Si resonators compared with gold nanoparticles, where the high Ohmic loss can significantly reduce the PL intensity.⁴³ In this way, although the emission rate of PNCs is reduced at room temperature by nonradiative channels, an outstanding improvement of the PL is demonstrated. The determination of the Purcell effect by time resolved PL (TRPL) characterization is, however, limited here due to the influence nonradiative recombination in the kinetics spectra at room temperature, which reduces the effective lifetime to <1 ns with and without the influence of the Mie scatters (not shown).

We now consider the coupling between Mie resonators and PNCs as a tool for enhancing the sensitivity in absorption measurements of individual nanocrystals. Following Ref. 44, for a single PNC, we have $\sigma/A = 1 - T$, where A is the size of the detection spot and σ is the PNC absorption cross section. This formula has a simple geometrical meaning: the absorption by a nanoparticle determines an opaque area through which light cannot pass. In other words, the transmission T goes to zero whenever A is comparable to σ .⁴⁴ We compare PL and scattering spectra for four different points where the PNCs and the titania spheres are spatially aligned (Fig. 4). Here, the alignment is determined optically by observing the dark-field scattering and the PL at the same point. The spatial matching is checked by collecting the two images on the same optical system, with few seconds delay, and comparing the optical images with an estimated resolution of ~ 200 nm. In addition, PL intensity (centered on the range 510–530 nm) experiences a strong enhancement at these spatial points, thus confirming a near-field coupling between the Mie antenna and the PNC. Dark-field scattering spectra are obtained by illuminating with a Tungsten lamp and are not corrected for the lamp spectrum or detector spectral band. In all these cases, a sharp reduction of the scattering of the Mie resonator is observed exactly at the position where the PL lines are located, which is clearly due to the influence of the perovskite absorption edge. It is worth stressing that we picked up four different PNCs with different central wavelengths of the PL band to confirm the link between the sharp reduction in the resonant scattering and the PNC exciton transition. In addition, the amplitude of the absorption step changes in different cases and always remains quite large: from 10% to more than 70%. We expect that the main reason for this large variation in the amplitude of the absorption step is due to the fact that

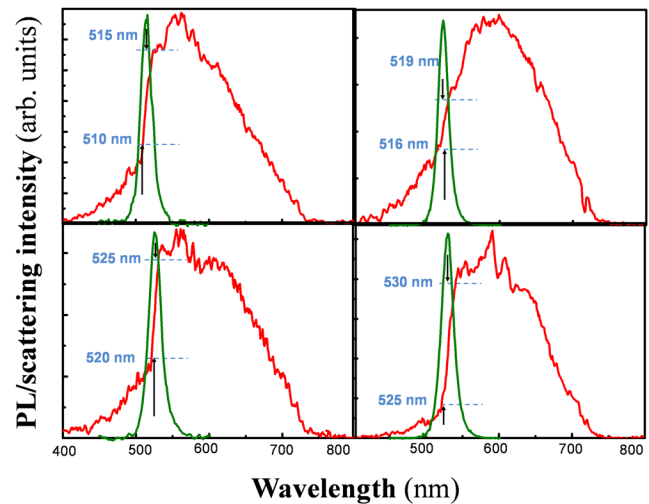


FIG. 4. Scattering and PL spectra for PNC–Mie systems with different PNC exciton transitions ranging from 515 nm to 530 nm. Note the clear reduction in the scattering for wavelengths smaller than the exciton transition wavelength compared to the spectra shown in Fig. 1(d). The size of the step also changes, denoting differences in the size and position of the PNCs, as discussed in the text.

(as deduced from SEM analysis; Figs. 2 and 3) the Mie resonator can be decorated by one (small steps) or a few PNCs (large steps). Other possibilities reside in the different sphere–PNP coupling, both spectral and spatial.

Although the precise number of PNCs decorating each sphere is unknown, different central wavelengths of the PL bands and the corresponding absorption edges account for the presence of a limited number of nanoparticles. This observation denotes the strength of our approach in detecting absorption from individual (or, at most, a few) PNCs. We also note that the absorption is very large and well resolved in the raw data presented in Fig. 4, indicating the possibility of performing single object nanoscopy using dielectric antennas even in the case of systems with smaller nanoemitter size and/or reduced oscillator strength. Here, the influence of the scattering of PNCs in the spectra is absolutely discarded since the size of these nanoparticles is much smaller than the Mie resonator.³⁹

Here, we simultaneously exploit two important features of Mie resonators, the first of which is the enhancement of the absorption cross section via the so-called surface enhanced absorption (SEA). This phenomenon was recently demonstrated in the system formed by organic dye molecules coupled to plasmonic nanoantennas and owes its denomination to the well-known SEF and SERS (surface enhanced Raman scattering) effects. It is simply the absorption counterpart of the Purcell effect observed in emission; that is, whenever the light–matter interaction leads to enhancement of the radiative rate, an identical enhancement is expected in the absorption cross section. Note that SEA may occur at a different wavelength to SEF when a large Stokes shift between emission and absorption is present (e.g., as in many organic molecules). However, for the selected PNCs we analyzed previously, almost no Stokes shift is present [Fig. 2(c)].

Second, as previously stated, a way to increase the absorption visibility is by reducing the detection spot size A . For example, this approach has been demonstrated in confocal microscopy,⁴⁵ scanning near-field microscopy,⁴⁶ and plasmonic systems.⁴⁷ In our case, the guided light in the glass substrate couples to the dielectric spheres in the near-field and scatter light into the far-field. Whenever a PNC is near to a Mie resonator, the exciton absorption reduces the scattering over the corresponding spectral range. In other words, this dark-field configuration is also a simple and suitable method to reduce A to the size of the Mie resonator, which is well below λ^2 .

In order to check and understand the experimental results shown above, we performed finite-difference time-domain (FDTD) simulations of the far-field scattering from titania spheres with and without PNCs. In all simulations, the size of the PNC is 100 nm and that of the sphere diameter is 300 nm. We recorded the optical power scattered above the glass slide such that it could be collected by the microscope objective in the far-field with a numerical aperture of 0.87 (60° around the surface normal). In order to simulate the effect of a semi-infinite glass slide, several simulations are combined using different glass substrate thicknesses, as described in the Experimental Methods section. However, the absolute thickness of the glass slab is not relevant for the scattering spectrum lineshape with or without the presence of a PNC (aside a slight variation in the scattered peak intensities). Therefore, for selected simulations, we use only a single substrate thickness of 100 nm in order to reduce the simulation time. We further note that the scattering spectra in Figs. 5(a) and 5(b) do not take into account the spectral distribution of the source power used in the experimental measurements, which in practice limits the usable spectral range to between 450 nm and 750 nm, thereby covering only the two lowest order Mie resonances around 500 nm and 650 nm.

In Fig. 5(a), we analyze the role of a single PNC both with and without the Mie resonator, considering different geometric configurations. The simulations show that for PNCs of the order of 100 nm (or smaller), there is no Mie scattering by the PNC itself within the wavelength range considered. Coupling the PNC to the Mie sphere, we found that the position of the PNC with respect to the direction of the incoming light is quite relevant: only with the PNC sitting in front of the sphere, we can observe the absorption edge. In fact, the

scattering intensity in the two configurations “behind” and “side” just reveals the scattering of the titania sphere, with the expected intense and broad Mie resonances.

Given the possibility of having multiple PNCs coupled with a single Mie sphere, we simulated different configurations with two (“bis” schemes) and three (“tris” schemes) PNCs, as shown in Fig. 5(b). In this case, the arrangement of the PNCs is once again relevant in determining the visibility of the absorption edge. It is also worth stressing that the simulations highlight the non-intuitive effect that the intensity of the absorption effect does not scale linearly with the number of PNCs attached to a resonator. This is likely due to the simultaneous modification of the Mie scattering by the composite structure (titania and perovskite have similar real dielectric constants), making the picture more complex. Nonetheless, the absorption of one PNC or a few PNCs can be easily detected in our dark-field configuration, exploiting the near-field interaction of the PNC excitonic transition with the dielectric antennas. We note that the antennas may also have an important steering effect on both the PL emission and the elastic scattering. An exhaustive study of this point is outside the scope of this paper. However, we find (not shown here) that the angular pattern of the Mie scattering of the guided modes in the glass slide is modified by changing the scale factor a/λ (a is the radius of the titania sphere), proving that nanoscopy by dielectric nano-antennas is indeed broadband and can be optimized still further by carefully tuning particular Mie resonances to the exciton transition wavelength. This would provide an additional enhancement in the collected PL by a preferable directionality of the scattered light to the normal direction. Indeed, this additional enhancement has a different physical nature than that occurred by the strong near field and would not modify the radiative lifetime of the system. Here, it is worth mentioning that the proposed experimental setup is ideal to collect all PL contributions: a different system (i.e., an integrated sphere) would prevent the detection of this second enhancement due to directionality.

Finally, in order to make an easier comparison with the experimental data, Fig. 5(c) reports the scattering for the “in front” configuration by considering the actual spectral lineshape of the lamp used in the experiment. This simulation shows a scattering lineshape with a clear step at the PNC exciton transition, quite similar to the ones observed experimentally [for instance, see Fig. 3(b)]. In some

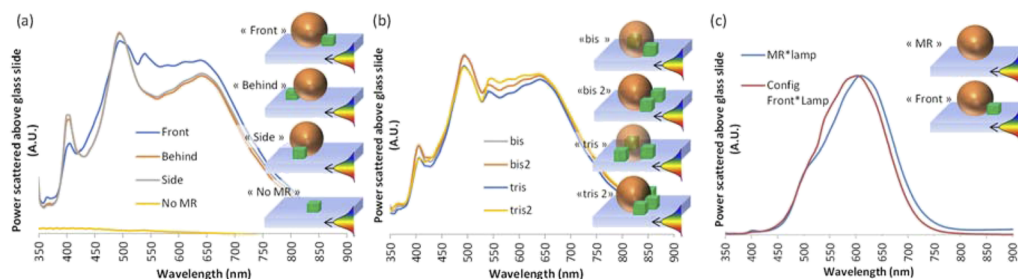


FIG. 5. Scattering coefficient describing power above the substrate for a wavelength independent source for different configurations with respect to the incident light direction for a 300 nm diameter Mie resonator and (a) a single PNP cube of 100 nm side and (b) two or three PNP cubes. (c) Power scattered above the substrate taking into account the true lamp spectrum for a lone MR and the “front” configuration from (a). The arrows highlight the position of the absorption edge of the PNCs.

cases, the experimental data still show very pronounced steps [see Fig. 3(d)], which suggests cases with either an extended clustering of PNCs or a larger SEA effect (or both). Even if full understanding of the actual magnitude of the experimental absorption step in each case would require additional information (which so far is missing, such as the sphere diameter, the number, size, and position of the PNCs, the SEA effect for each of them, etc.), both the experimental data and the simulations point to the soundness, reliability, and simplicity of the use of Mie antennas for efficient and inexpensive optical nanoscopy.

In Fig. 6(a), the near-field enhancement factor is calculated for all wavelengths, indicating the average optical intensity enhancement within the PNC volume when the PNCs are placed on the substrate at the base of the MR with respect to when they are placed on a bare section of the substrate. It can be seen that at wavelengths for which Mie resonances occur within the spectral range of interest, enhancements of up to a factor of two and five occur. The final and most important factor affecting the collection of light above the plane of the substrate is, as discussed previously, the scattering effect of the MRs at resonance, which serves to extract photons otherwise bound by total internal reflection in the substrate such that a high optical power is radiated toward the collection objective. Figure 6(b) shows the real part of the near-field distribution of the transverse component of the electric field, i.e., oriented perpendicular to the plane of the monitor, in the vicinity of the MR. Plots have been shown for free space wavelengths corresponding to resonances in the MR [maxima of the Scattering coefficients in Figs. 5(a) and 5(b)]: the dipolar, quadrupolar, and octopolar resonances are found at 670 nm, 510 nm, and 405 nm, respectively. In the lower part of the plots, the surface of the glass slide (here of a thickness of 100 nm, permitting the best excitation of the Mie resonances for all thicknesses considered) is visible and the periodic field distribution of the propagating guided mode is clearly evident. When this periodic field encounters the MR, it couples to the electric field corresponding to the Mie resonances, which we remind the reader are simply low-order whispering gallery modes and therefore occur at optical frequencies, for which the wavelength of light within the MR (i.e., the free-space wavelength divided by the MR refractive index) is equal to the MR circumference in the plane of the monitor divided by an integer. Indeed, a partial phase-matching phenomena can be seen between the periodic field in the MR and that in

the glass substrate that is not perfect due to the mismatch in the modal index of the guided mode and the material refractive index of the MR. Light in the Mie resonances is subject to constructive interference on round trips around the MR circumference, and so the lifetime of photons within these modes is enhanced, leading to the first element of the explanation for the increased interaction with the neighboring PNC cluster. A further part of the explanation for the increased light-matter interaction between photons in the Mie resonances and the perovskite material is due to the overlap of the evanescent field of the resonances with the PNC cluster.

Our approach can be easily extended to other exciton transitions in different nano-systems, including quantum emitters. With respect to the vast literature of plasmonics in this field, dielectric sub-micrometric antennas clearly show advantages and disadvantages, as largely discussed in many publications.¹¹ Therefore, here, we skip to further discuss this point, limiting the state of the art comparison to Mie resonators coupled to nanoparticles. Recently, examples of exploitation of dielectric sub-micrometric antennas have been published, demonstrating PL enhancement from quantum dots¹¹ with engineered Si-based disks providing a spectral overlap of electric and magnetic dipolar modes for optimal emission yield. Similarly, Bohn *et al.* recently reported PL enhancement by tailored dielectric metasurfaces.⁴⁸ Our approach shows similar PL enhancement exploiting a bottom-up approach that is low cost and easily scalable to large surfaces, allowing us to fabricate the antennas as well as spatially coupling them to the emitters. Tailored Si nanospheres have been recently used for enhancing the CdSe/ZnS QD PL by a factor of two.⁴⁹ They exploited surface adhesion of the colloidal QDs by electrostatic forces, obtaining more than 2000 emitters linked to a single dielectric antenna, which is clearly interesting, but far from a nanoscopy approach for single exciton detection. All these reports used sub-micrometric antennas based on Si due to the large refractive index of this material. Therefore, it is worth stressing that the relatively low refractive index of titania with respect to silicon could even be useful. Indeed, few materials allow for a broader band response and a larger spectral interval of electric and magnetic dipolar resonance overlap,^{28,50} which is a clear advantage in addition to the obvious absence of absorption in titania in the visible with respect to conventional Si, Ge dielectric antennas, and plasmonic particles.

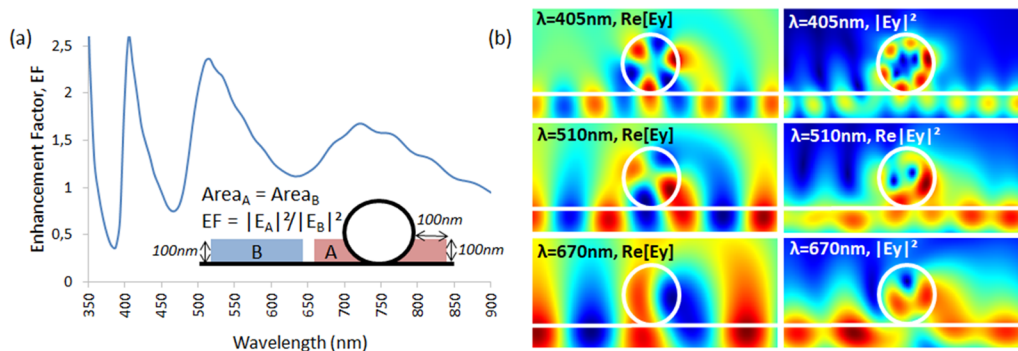


FIG. 6. (a) Calculation of the enhancement factor spectra. (b) Electric field distribution for different wavelengths.

We close the comparison with the literature by discussing the observed Fano-like enhancement of the excitonic transition superimposed on the intrinsic Mie resonance spectra in large spherical PNCs fabricated by laser ablation.³² Although the integration of excitonic and Mie resonances in the same sub-micrometric cluster is very interesting, it has evident limits as a general purpose nanoscopy tool as it cannot be used as an independent substrate to disperse any kinds of emitter particles or more complex nano-bio-systems. In addition, the quality of the nanosphere obtainable from laser ablation is not optimal, which, linked with the unavoidable loss due to reabsorption, makes the use of a perovskite nanoantenna not ideal. Our method, involving real dielectric materials and bottom-up synthesis, provides smooth and spherical sub-micrometric antennas (roughness $\sim\lambda/50$) dispersed on any substrate, allowing one to address any excitonic transition (and to have larger PL enhancement than Ref. 32 in PNCs) when just one PNC is attached to the microsphere, and demonstrates a simple dark-field scattering measurement system for absorption nanoscopy.

In summary, we have demonstrated that the combination of chemical synthesis/deposition of absorption free and high-quality titania dielectric antennas and optical microscopy in both bright- and dark-field geometry can be exploited as an efficient far-field nanoscopy optical tool for addressing excitonic transitions in individual PNCs. Our method merges some advantages of near-field approaches (usually performed by complex and expensive SNOM setup) and the simplicity and low-cost nature of standard spectroscopic microscopy (even without extreme spatial resolution). A relevant enhancement of the PL emission has been obtained from the technologically interesting system of CsPbBr₃ PNCs, and we have demonstrated the possibility to implement sensitive absorption measurements at the nanoscale addressing individual PNCs with unprecedented sensitivity.

Of the utmost relevance for the uptake of our approach in different systems is its scalability and the limited technological requirements for fabricating and depositing the antennas, as well as implementing the micro-spectroscopic setup. The simplicity and low cost of this nanoscopy tool leads us to believe that it could pave the way for detecting the somewhat elusive absorption signal of single exciton in many recently proposed nano-sized quantum emitters, expected to be the building blocks for the new quantum revolution in communication and computing. In this scenario, we would like to stress that Mie sub-micrometric antennas (if carefully designed, which is not the aim of this report) can efficiently produce very specific far-field angular steering (by fully exploiting the interference between electric and magnetic resonances), thereby optimizing and tailoring detection sensitivity. Future experiments will include angular resolved studies to determine the directionality of the scattered light and time resolved PL at cryogenic temperatures to obtain an accurate value of the Purcell Factor without the limitation of the nonradiative channels.

EXPERIMENTAL METHODS

Titania spheres were obtained by the following procedure (see also Ref. 34): all chemical precursors were provided by Sigma Aldrich and used as received. The titania spheres were obtained

by atomizing a hydro-alcoholic solution (1:TiCl₄, 20:EtOH, and 5:H₂O molar fractions) in an air flux using an aerosol generator (TOPAZ ATM 210). The solution droplets were carried with the air flux and channeled into a furnace at 300 °C for a few seconds to complete the evaporation of volatile species and to consolidate the sphere shell via condensation. The pre-stabilized spherical particles were then ejected through a nozzle at the furnace exit, in front of which substrates (either microscope glass slides or silicon wafers) were positioned. The accelerated particles/air mixture was allowed to have impact on the substrates for just a few seconds so as to yield particle deposition in a highly dispersed configuration, thus avoiding the presence of aggregated clusters, as required for an easy spectroscopic characterization with a confocal microscope. The substrates supporting the spheres were then heated at 450 °C for 10 min to trigger the final densification and crystallization of the spheres. The same sol-gel solution was used to prepare a homogeneous coating on Si wafers by dip-coating (ACEdip equipment from Solgelway). After the same thermal treatment, the final stiff TiO₂ coating is expected to exhibit the same optical constants as the spheres. Spectroscopic ellipsometry (Woollam M2000V) was used to measure the dispersion of the refractive index n and extinction coefficient k of the titania composing the spheres. The best fit was found with a Cauchy dispersion model [$k = 0$ and $n(\lambda) = A + B/\lambda^2$ (with $A = 2.007$, $B = 0.058$)], which gives $n = 2.293$ at 450 nm.

The hot-injection method was carried out for the preparation of CsPbBr₃ PNCs, applying some modifications.² No additional purification treatments were performed to the reactants, which were used as received. In a typical synthesis, 0.41 g Cs₂CO₃ (Sigma-Aldrich, 99.9%) and 1.25 ml of oleic acid (OA, Sigma Aldrich, 90%) were mixed with 20 ml of 1-octadecene (1-ODE, Sigma-Aldrich, 90%) into a 50 ml-three neck, in order to prepare a Cs-oleate solution. The mixture was constantly stirred at 120 °C under vacuum conditions for 1 h. Then, the mixture was heated to 150 °C under the N₂ atmosphere until complete dissolution of Cs₂CO₃ occurred. To prevent the formation of Cs₂O as an oxidation product, the temperature of solution was kept at 100 °C under continuous N₂-purge.

Separately, 0.69 g PbBr₂ (ABCR, 99.999%) and 50 ml of 1-ODE were mixed into a 100 ml-three neck flask under vacuum for 1 h, with constant stirring at 120 °C. Then, under the N₂ atmosphere, 5 ml of both OA and oleylamine (OLA, Sigma-Aldrich, 98%) were separately added to the flask, while increasing the temperature rapidly to 170 °C. At this point, 4 ml of Cs-oleate solution was quickly injected. Finally, the reaction mixture was quenched by immersing the flask into an ice bath for 5 s, achieving a green colored colloidal solution. Perovskite NPs were isolated by centrifuging the colloidal solution at 4700 rpm for 10 min. The supernatant was discarded to obtain the NPs pellets, which were then re-dispersed in hexane to prepare a stock solution of 50 mg ml⁻¹.

Prior to the deposition of the PNCs, samples were carefully cleaned with acetone, ethanol, and isopropanol during 10 min in an ultrasound bath. Then, PNCs were deposited on the titania spheres by immersing the samples in the appropriate solution and drying with compressed air. In these conditions, PNC density can be controlled by the immersion time (10–30 min) and their concentration in hexane (0.5–5 mg ml⁻¹).

Morphological studies of titania spheres, PNCs and also the two structures coupled together, were performed by high-resolution SEM. We use a FEI Helios 600 NanoLab using a through-the-lens detector (TLD) of secondary electrons, 5 kV acceleration voltage, 0.17 nA probe current, and 4.2 mm working distance. To increase the sample conductivity and hence perform better SEM imaging, the spheres and the nanocrystals were deposited on a silicon substrate, instead of on glass slides as for the optical study. However, we take care to have a layer of SiO₂ on top of the Si substrate (native oxide, few nm thick) where the titania and then the NPN are deposited. This ensures that the chemistry leading to deposition, migration, adhesion, and aggregation is almost the same for glass slides and Si wafers.

Optical studies were performed in a custom-made microscopy setup, allowing for simultaneous detection of the optical image of the sample (with a DCU224M CCD camera from Thorlabs), the PNC photoluminescence, and the elastic scattering by titania spheres. An $\sim 3 \mu\text{m}$ lateral resolution was achieved by simultaneously collecting the light scattering and PL emission with a 50 \times objective lens (NA = 0.43) and filtering them with an optical fiber (core of 50 μm). Light detection was performed with an Ocean Optics USB-650 spectrometer. PL emission was excited by a continuous-wave GaN laser at 404 nm at grazing incidence on the sample defining a spot of several mm in diameter. This ensures a uniform excitation and the possibility of using a large field of view in all the spectroscopic measurements.

Dark-field microscopy and spectroscopy were performed by coupling white light from a Tungsten lamp into the glass slide substrates via lateral illumination. Since images were collected from the above sample (i.e., at normal incidence with respect to the glass plane), we only had signal coming from the scattering sites located on the surface, i.e., mainly from the titania spheres. The use of a simultaneous illumination by the guided white light and a laser beam at grazing incidence allowed us to spatially correlate the position of Mie resonators and PNCs.

Three-dimensional FDTD simulations were performed using the commercial software (Lumerical FDTD Solutions). A titania sphere of diameter 300 nm (and/or PNCs in the configurations described in the main text) was placed on a glass (silica) slab waveguide occupying the full simulation space in the xy plane and of variable thickness in the z direction. A scattered power monitor was placed above the sphere (covering the full xy plane), with the dimensions being such that light radiated into a cone of 60° above the plane of the glass slide would be detected. The full simulation volume was bounded with perfectly matched layers to absorb outgoing light, and the spatial resolution was 25 nm except in a 400 nm cube around the MR, for which the resolution was increased to 20 nm. Optical power was injected into the fundamental guided mode of the glass slab in the +x direction over the wavelength range 300–900 nm. In order to simulate a glass substrate of infinite thickness in which optical power is evenly distributed at propagation angles between the critical angle ($\sim 45^\circ$) and 90° with respect to the surface normal, the thickness of the glass slab was varied and the fundamental mode profile recalculated for each thickness. In this way, the angle of incidence (AoI) of light impinging on the interfaces of the slide varies between the critical angle for an infinitely thin waveguide (TE mode case, for which there is no cutoff thickness), and 90° for an infinitely thick one. In practice, the waveguide

thickness was swept between 100 nm (AoI = 48° at 650 nm wavelength) and 2000 nm (AoI = 87° at 650 nm wavelength), and the scattering from the MR (+PNCs) toward the power monitor was weighted for each waveguide thickness to take into account the differences in surface field intensity and the effective AoI range represented.

The refractive index dispersion in the wavelength range of interest came from the ellipsometry investigation and the literature for aerosol TiO₂³⁴ and from the literature only for PNCs, since a homogeneous layer of such a perovskite cannot be obtained.⁵¹ We note that the imaginary part of the PNC refractive index was linearly scaled by a factor of two, justified by the fact that the perovskite studied in the literature was in the form of a thin film, whereas it is in the form of nanocrystals in the present work, which can lead to an enhanced absorption due to quantum size effects. In any case, the bandgap wavelength giving rise to the clear absorption edge seen is identical to the literature value. A complete characterization of these aspects is largely beyond the scope of this paper, which is to highlight the soundness and simplicity of the use of Mie antennas for efficient and inexpensive optical nanoscopy.

ACKNOWLEDGMENTS

The authors acknowledge funding from the Spanish MICINN (Grant No. TEC2017-86102-C2-1-R), Laserlab-Europe ARES (No. 654148) funded by the European Union, the PRCI network ULYSSES (No. ANR-15-CE24-0027-01) funded by the French ANR agency, the A*MIDEX foundation (ANR-11-IDEX-0001-02), the A*MIDEX Project TITANIDE (No. A-M-AAP-EI-17-58-170228-16.21-ABBARCHI-SAT), and the Prometeo/2018/098 (Q-Devices) funded by Generalitat Valenciana and the FET-OPEN project NARCISO (No. 828890). S.C. acknowledges the COST action (MP1403). M.G. acknowledges the CNRS (France) for supporting his permanence at the IM2NP Institute of Marseille. We acknowledge the facilities of the NANOTECHMAT platform at the IM2NP Institute and of the microscopy center CP2M of Aix-Marseille University.

REFERENCES

- ¹J. Huang, Y. Yuan, Y. Shao, and Y. Yan, *Nat. Rev. Mater.* **18**, 17042 (2017).
- ²L. Protesescu, S. Yakunin, M. I. Bodnarchuk, F. Krieg, R. Caputo, C. H. Hendon, R. X. Yang, A. Walsh, and M. V. Kovalenko, *Nano Lett.* **15**, 3692 (2015).
- ³P. Fu, Q. Shan, Y. Shang, J. Song, H. Zeng, Z. Ning, and J. Gong, *Sci. Bull.* **62**, 369 (2017).
- ⁴Q. A. Akkerman, M. Gandini, F. Di Stasio, P. Rastogi, F. Palazon, G. Bertoni, J. M. Ball, M. Prato, A. Petrozza, and L. Manna, *Nat. Energy* **2**, 16194 (2017).
- ⁵J. Pan, S. P. Sarmah, B. Murali, I. Dursun, W. Peng, M. R. Parida, J. Liu, L. Sinatra, N. Alyami, C. Zhao, E. Alarousu, T. K. Ng, B. S. Ooi, O. M. Bakr, and O. F. Mohammed, *J. Phys. Chem. Lett.* **6**, 5027 (2015).
- ⁶T. Yang, Y. Zheng, Z. Du, W. Liu, Z. Yang, F. Gao, L. Wang, K. C. Chou, X. Hou, and W. Yang, *ACS Nano* **12**, 1611 (2018).
- ⁷A. Ferrando, J. P. Martínez-Pastor, and I. Suárez, *J. Phys. Chem. Lett.* **9**, 5612 (2018).
- ⁸L. Novotny and N. van Hulst, *Nat. Photonics* **5**, 83 (2011).
- ⁹M. Signoretto, N. Zink-Lorre, J. P. Martínez-Pastor, E. Font-Sanchis, V. S. Chirvony, Á. Sastre-Santos, F. Fernández-Lázaro, and I. Suárez, *Appl. Phys. Lett.* **111**, 081102 (2017).
- ¹⁰P. Törmä and W. L. Barnes, *Rep. Prog. Phys.* **78**, 013901 (2014).

- ¹¹I. Staude, T. Pertsch, and Y. S. Kivshar, *ACS Photonics* **6**, 802 (2019).
- ¹²M. Li, S. K. Cushing, and N. Wu, *Analyst* **140**, 386 (2015).
- ¹³S. Balci, E. Karademir, C. Kocabas, and A. Aydinli, *Opt. Lett.* **39**, 4994 (2014).
- ¹⁴E. A. Wertz, B. P. Isaacoff, and J. S. Biteen, *ACS Photonics* **3**, 1733 (2016).
- ¹⁵A. E. Krasnok, I. S. Maksymov, A. I. Denisjuk, P. A. Belov, A. E. Miroschnichenko, C. R. Simovski, and Y. S. Kivshar, *Phys.-Usp.* **56**, 539 (2013).
- ¹⁶A. E. Krasnok, A. E. Miroschnichenko, P. A. Belov, and Y. S. Kivshar, *Opt. Express* **20**, 20599 (2012).
- ¹⁷A. E. Krasnok, C. R. Simovski, P. A. Belov, and Y. S. Kivshar, *Nanoscale* **6**, 7354 (2014).
- ¹⁸J. A. Schuller, R. Zia, T. Taubner, and M. L. Brongersma, *Phys. Rev. Lett.* **99**, 107401 (2007).
- ¹⁹A. B. Evlyukhin, S. M. Novikov, U. Zywiets, R. L. Eriksen, C. Reinhardt, S. I. Bozhevolnyi, and B. N. Chichkov, *Nano Lett.* **12**, 3749 (2012).
- ²⁰R. C. Devlin, M. Khorasaninejad, W.-T. Chen, J. Oh, and F. Capasso, *Proc. Natl. Acad. Sci. U. S. A.* **113**, 10473 (2016).
- ²¹A.-Y. Choi, Y. S. Kivshar, D. N. Neshev, M. Liu, H. Altug, A. Tittl, F. Yesilkoy, and A. Leitis, *Science* **360**, 1105 (2018).
- ²²Y. Yang, W. Wang, A. Boulesbaa, I. I. Kravchenko, D. P. Briggs, A. Puztzyk, D. Geoghegan, and J. Valentine, *Nano Lett.* **15**, 7388 (2015).
- ²³P. Spinelli, M. A. Verschuuren, and A. Polman, *Nat. Commun.* **3**, 692 (2012).
- ²⁴P. Moitra, B. A. Slovick, Z. Gang Yu, S. Krishnamurthy, and J. Valentine, *Appl. Phys. Lett.* **104**, 171102 (2014).
- ²⁵R. C. Devlin, M. Khorasaninejad, F. Capasso, A. Y. Zhu, W. T. Chen, and J. Oh, *Science* **352**, 1190 (2016).
- ²⁶Y. Yang, W. Wang, P. Moitra, I. I. Kravchenko, D. P. Briggs, and J. Valentine, *Nano Lett.* **14**, 1394 (2014).
- ²⁷D. Lin, P. Fan, E. Hasman, and M. L. Brongersma, *Science* **345**, 298 (2014).
- ²⁸I. Staude, V. V. Khardikov, N. T. Fofang, S. Liu, M. Decker, D. N. Neshev, T. S. Luk, I. Brener, and Y. S. Kivshar, *ACS Photonics* **2**, 172 (2015).
- ²⁹E. Tiguntseva, A. Chebykin, A. Ishteev, R. Haroldson, B. Balachandran, E. Ushakova, F. Komissarenko, H. Wang, V. Milichko, A. Tsyppkin, D. Zuev, W. Hu, S. Makarov, and A. Zakhidov, *Nanoscale* **9**, 12486 (2017).
- ³⁰S. V. Makarov, V. Milichko, E. V. Ushakova, M. Omelyanovich, A. Cerdan Pasaran, R. Haroldson, B. Balachandran, H. Wang, W. Hu, Y. S. Kivshar, and A. A. Zakhidov, *ACS Photonics* **4**, 728 (2017).
- ³¹E. Y. Tiguntseva, G. P. Zograf, F. E. Komissarenko, D. A. Zuev, A. A. Zakhidov, S. V. Makarov, and Y. S. Kivshar, *Nano Lett.* **18**, 1185 (2018).
- ³²D. G. Baranov, S. V. Makarov, A. P. Pushkarev, M. Franckevičius, Y. S. Kivshar, E. Y. Tiguntseva, A. A. Zakhidov, T. Shegai, F. Komissarenko, and B. Munkhbat, *Nano Lett.* **18**, 5522 (2018).
- ³³A. S. Berestennikov, P. M. Voroshilov, S. V. Makarov, and Y. S. Kivshar, *Appl. Phys. Rev.* **6**, 031307 (2019).
- ³⁴S. Checucci, T. Bottein, J. B. Claude, T. Wood, M. Putero, L. Favre, M. Gurioli, M. Abbarchi, and D. Grosso, *Adv. Funct. Mater.* **28**, 1801958 (2018).
- ³⁵A. F. Gualdrón-Reyes, S. J. Yoon, E. M. Barea, S. Agouram, V. Muñoz-Sanjosé, Á. M. Meléndez, M. E. Niño-Gómez, and I. Mora-Seró, *ACS Energy Lett.* **4**, 54 (2019).
- ³⁶B. T. Diroll, H. Zhou, and R. D. Schaller, *Adv. Funct. Mater.* **28**, 1800945 (2018).
- ³⁷M. Abbarchi, F. Troiani, C. Mastrandrea, G. Goldoni, T. Kuroda, T. Mano, K. Sakoda, N. Koguchi, S. Sanguinetti, A. Vinattieri, and M. Gurioli, *Appl. Phys. Lett.* **93**, 162101 (2008).
- ³⁸M. C. Brennan, J. Zinna, and M. Kuno, *ACS Energy Lett.* **2**, 1487 (2017).
- ³⁹A. S. Berestennikov, Y. Li, I. V. Iorsh, A. A. Zakhidov, A. L. Rogach, and S. V. Makarov, *Nanoscale* **11**, 6747 (2019).
- ⁴⁰F. Di Stasio, J. Q. Grim, V. Lesnyak, P. Rastogi, L. Manna, I. Moreels, and R. Krahne, *Small* **11**, 1328 (2015).
- ⁴¹S. Kühn, U. Håkanson, L. Rogobete, and V. Sandoghdar, *Phys. Rev. Lett.* **97**, 017402 (2006).
- ⁴²C. Cai, X. Wang, L. Ling, G. Bi, Z. Xu, and H. Wu, *Opt. Lett.* **44**, 658 (2019).
- ⁴³S. V. Gaponenko, P. M. Adam, D. V. Guzatov, and A. O. Muravitskaya, *Sci. Rep.* **9**, 7138 (2019).
- ⁴⁴G. Zumofen, N. M. Mojarad, V. Sandoghdar, and M. Agio, *Phys. Rev. Lett.* **101**, 180404 (2008).
- ⁴⁵A. Högele, S. Seidl, M. Kroner, K. Karrai, C. Schulhauser, O. Sqalli, J. Scrimgeour, and R. J. Warburton, *Rev. Sci. Instrum.* **79**, 023709 (2008).
- ⁴⁶I. Gerhardt, G. Wrigge, P. Bushev, G. Zumofen, M. Agio, R. Pfab, and V. Sandoghdar, *Phys. Rev. Lett.* **98**, 033601 (2007).
- ⁴⁷B. L. Darby, B. Auguie, M. Meyer, A. E. Pantoja, and E. C. Le Ru, *Nat. Photonics* **10**, 40 (2015).
- ⁴⁸J. Bohn, T. Bucher, K. E. Chong, A. Komar, D. Y. Choi, D. N. Neshev, Y. S. Kivshar, T. Pertsch, and I. Staude, *Nano Lett.* **18**, 3461 (2018).
- ⁴⁹X. Yang, Y. Li, and B. Li, *ACS Photonics* **4**, 2669 (2017).
- ⁵⁰A. Garcia-Etxarri, R. Gomez-Medina, L. S. Froufe-Perez, C. Lopez, L. Chantada, F. Scheffold, J. Aizpurua, M. Nieto-Vesperinas, and J. J. Saenz, *Opt. Express* **19**, 4815 (2010).
- ⁵¹M. Sharizal Alias, I. Dursun, M. I. Saidaminov, E. Marwane Diallo, P. Mishra, T. N. Khee, O. M. Bakr, and B. S. Ooi, *Opt. Express* **24**, 201 (2016).